

Hard X-ray emission of the Earth’s atmosphere: Monte Carlo simulations

S. Sazonov^{1,2*}, E. Churazov^{1,2}, R. Sunyaev^{1,2} and M. Revnivtsev^{1,2}

¹*Max-Planck-Institut für Astrophysik, Karl-Schwarzschild-Str. 1, 85740 Garching bei München, Germany*

²*Space Research Institute, Russian Academy of Sciences, Profsoyuznaya 84/32, 117997 Moscow, Russia*

14 July 2021

ABSTRACT

We perform Monte Carlo simulations of cosmic ray-induced hard X-ray radiation from the Earth’s atmosphere. We find that the shape of the spectrum emergent from the atmosphere in the energy range 25–300 keV is mainly determined by Compton scatterings and photoabsorption, and is almost insensitive to the incident cosmic-ray spectrum. We provide a fitting formula for the hard X-ray surface brightness of the atmosphere as would be measured by a satellite-born instrument, as a function of energy, solar modulation level, geomagnetic cutoff rigidity and zenith angle. A recent measurement by the INTEGRAL observatory of the atmospheric hard X-ray flux during the occultation of the cosmic X-ray background by the Earth agrees with our prediction within 10%. This suggests that Earth observations could be used for in-orbit calibration of future hard X-ray telescopes. We also demonstrate that the hard X-ray spectra generated by cosmic rays in the crusts of the Moon, Mars and Mercury should be significantly different from that emitted by the Earth’s atmosphere.

Key words: Earth – gamma-rays: observations – X-rays: diffuse background – Moon

1 INTRODUCTION

Starting in the 1960’s, observations from balloons (Peterson et al. 1973; Daniel & Stephens 1974; Schönfelder et al. 1980) and spacecraft (Golenetskii et al. 1974; Schwartz & Peterson 1974; Imhof et al. 1976; Willett & Mahoney 1992; Share & Murphy 2001; Shaw et al. 2003) have shown that the Earth’s atmosphere is bright in hard X-rays and gamma-rays owing to its bombardment by cosmic rays of Galactic origin. This is the case despite the fact that the energy deposited by the cosmic rays into the atmosphere is some nine orders of magnitude smaller than the total energy budget coming to us from the Sun and that only $\sim 1\%$ of the energy deposited by the cosmic rays is re-radiated into space as gamma-rays and much less as hard X-rays.

Atmospheric hard X-ray emission is of interest not only because it provides insight into the interaction of energetic cosmic particles with air, but also in connection with the possibility of measuring the spectrum of the cosmic X-ray background (CXB) using the Earth as a shield. In January–February 2006 a series of observations following this approach were performed by the INTEGRAL orbital observatory (Churazov et al. 2007) and drew our attention to the problem of atmospheric X-ray radiation. In observa-

tions of this kind, cosmic ray-induced emission on the one hand causes significant contamination of the CXB decrement (due to occultation by the Earth) at energies ~ 30 –100 keV, but on the other, could in principle be used for calibrating a detector’s response in the high-energy region (substantially above 100 keV) where atmospheric emission dominates over the CXB signal. During the INTEGRAL observations the Earth covered ~ 100 sq. deg of the sky and was as bright as ~ 200 mCrab in the spectral band 100–200 keV (Churazov et al. 2007).

Despite the long history of experimental (see references above) and theoretical (Puskin 1970; Daniel & Stephens 1974; Ling 1975; Graser & Schönfelder 1977; Dean et al. 1989) studying, there remains significant uncertainty regarding the spectrum of atmospheric X-ray and gamma-ray radiation. However, the nuclear and electromagnetic processes responsible for the generation and propagation of X- and gamma-rays in the atmosphere, although complex, are well understood and already incorporated in computer codes. Also the incident energy spectrum of Galactic cosmic rays has been measured with high precision (see e.g. Gaisser et al. 2001 for a review) and there is a good understanding of how it is modified below ~ 10 GeV by the magnetic fields of the Solar system and Earth. All this suggests that the energy and angular distributions of atmospheric X-ray and gamma-ray emission should be predictable by simulations with fairly good ($\sim 10\%$) accuracy.

* E-mail: sazonov@mpa-garching.mpg.de

We have performed such a numerical modelling using the popular toolkit *GEANT* (Agostinelli et al. 2003), focusing on making predictions for observations of the Earth from space in the hard X-ray band 25–300 keV. We show below that the hard X-ray emission of the Earth is characterized by a well-defined spectral shape (Sect. 2) and that its intensity depends in a predictable way on the phase of the solar cycle and on the geomagnetic rigidity map corresponding to a given observation (Sect. 3). Therefore the Earth could become a good absolute calibrator for future orbital hard X-ray telescopes, in particular when used in combination with accurate monitoring of the cosmic-ray spectrum by large-area, high-resolution particle physics detectors such as the Alpha Magnetic Spectrometer to operate on the International Space Station (Barao et al. 2004).

In addition we demonstrate (Sect. 4) that the cosmic ray-irradiated solid crusts of the Moon, Mars and Mercury should generate hard X-ray spectra different from the one produced in the Earth’s atmosphere.

2 SIMULATIONS

Our Monte Carlo code is based on the *GEANT4* software package (release 8.1), which was developed at CERN as an extension of *GEANT3* and has many applications across particle physics and astronomy (Agostinelli et al. 2003). We adopted the physics model originally constructed for evaluating the effects of exposing the test masses of the Laser Interferometer Space Antenna to energetic particles in space (Araújo et al. 2005). This model includes a state-of-the-art description (in particular, intra-nuclear cascade models) of hadronic interactions of cosmic-ray protons and α -particles, and their air-shower products over many orders of magnitude in energy, as well as the low-energy electromagnetic package in *GEANT4*, which extends the standard electromagnetic package by carefully treating such processes as Rayleigh scattering, photoabsorption and fluorescence, important in the X-ray regime.

Unless otherwise stated, we use a plane-parallel approximation for the Earth’s atmosphere. Specifically, our adopted geometry is a slab of height 96 km and of very large (2×10^4 km) width and length. The air consists of atoms of nitrogen, oxygen and argon with mass fractions of 75.5%, 23.1% and 1.3%, respectively. The air’s density decreases exponentially with altitude from a sea-level value of 1.2 mg cm^{-3} with a scale height of 8 km. The total column density of our model atmosphere is thus $\sim 960 \text{ g cm}^{-2}$. This model is designed to approximate the real structure of the Earth’s atmosphere¹ below ~ 100 km. The remaining Earth’s atmosphere above this level is so rarefied ($\sim 1 \text{ mg cm}^{-2}$) that only a tiny fraction ($\lesssim 10^{-4}$) of the total X-ray and gamma-ray radiation escaping from the atmosphere into space is produced there, since the bulk of the emergent flux is produced in the upper several tens of g cm^{-2} of the atmosphere (above ~ 20 km from the sea level).

Importantly, by performing many test runs, we found that the properties of the emergent hard X-ray radiation remain unchanged within the statistical uncertainties if we

increase or decrease severalfold the total height, scale height, or the sea-level density of the atmosphere, as long as the total column density of the atmosphere remains higher than $\sim 200 \text{ g cm}^{-2}$. It is the chemical composition of the air that largely determines the outcome of simulations. Furthermore, we also carried out a series of simulations using a realistic spherical geometry for the atmosphere and convinced ourselves that the plane-parallel approximation is adequate for treating the problem under consideration (see Sect. 2.1 below).

We emphasize that we use our simulations to formulate predictions specifically for observations of the Earth from satellite orbits. This implies that the presented results should not be applied to observations performed from balloon (i.e. intra-atmospheric) altitudes.

2.1 Spectra induced by monoenergetic protons

We first performed a series of simulations in which the atmosphere was bombarded by monoenergetic protons. The protons were assumed to come from a uniform background subtending the 2π space above the atmosphere. This implies that the flux density of incoming particles $dF/d\mu \propto \mu$, where $\mu = \cos\theta$ and θ is the zenith angle. We accumulated the energy spectra (above an imposed threshold of 1 keV) and angular distributions of X- and gamma-rays produced in the proton-induced cascades and emergent from the atmosphere. Similar information was collected for the emergent electrons and positrons, to later assess the role of re-entrant albedo particles.

We typically sampled $(50,000\text{--}125,000)/E_p$ protons in a single run, where E_p (GeV) is the proton kinetic energy. By performing a number of test runs, we convinced ourselves that this number of sampled particles enables recovering outgoing hard X-ray to gamma-ray spectra (between ~ 25 keV and ~ 10 MeV) with a bin-to-bin statistical noise of less than 5% when a logarithmic grid of 10 energy bins per dex is used, and with a scatter in the amplitudes of spectra obtained in different runs of less than 3%. These levels of statistical uncertainty characterize all spectral plots presented below. We note that the accuracy of our simulations becomes significantly worse at photon energies below ~ 25 keV and above ~ 10 MeV (see in particular Fig. 3 below), in the regions lying outside the focus of this paper.

Figures 1 and 2 show the emergent zenith angle-integrated photon spectra for $E_p = 1$ and 10 GeV. One can see that several photon production mechanisms provide comparable contributions to the outgoing spectra. These include: i) free-free emission by electrons and positrons (distributed over several orders of magnitude in photon energy), ii) electron-positron annihilation (mostly in a line at 511 keV) and iii) high-energy processes including nuclear de-excitation (in the $\sim 1\text{--}15$ MeV range² and π^0 decay (a broad bump near 100 MeV). The energy albedo of the atmosphere (ratio of the emergent radiation flux over the incident energy flux of cosmic rays) ranges from $\sim 1\%$ for 1 GeV protons to $\sim 0.1\%$ for 250 GeV protons.

² Note that because of the short lifetimes (typically a tiny fraction of a second) of the excited state, atmospheric gamma-ray lines may be considered prompt (see e.g. Ramaty et al. 1979.)

¹ See e.g. <http://modelweb.gsfc.nasa.gov>

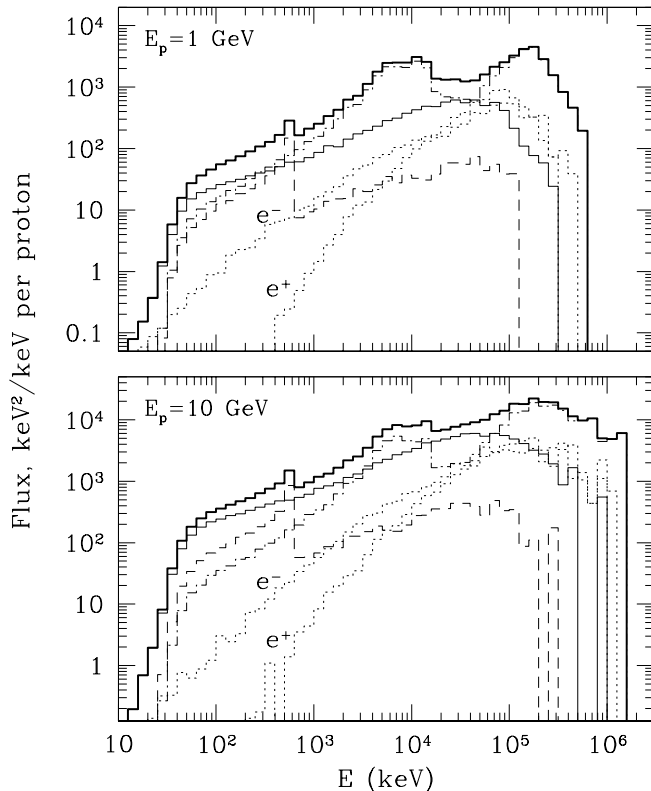


Figure 1. *Top:* Spectral energy distribution (in $E^2 dN_\gamma/dE$ units) of photons emergent from the atmosphere exposed from the top to an isotropic distribution of protons of energy $E_p = 1$ GeV. The thick solid line shows the total spectrum while the other lines show its different components according to the photon production process: free-free emission (solid), electron–positron annihilation (dashed), other processes including nuclear deexcitation and π^0 decay (dash-dotted). Also shown are the spectra ($E_e^2 dN_e/dE_e$) of secondary electrons and positrons escaping from the atmosphere (dotted). *Bottom:* The same but for $E_p = 10$ GeV.

As is evident from Fig. 2, most of the escaping photons with final energies below ~ 511 keV have experienced single or multiple Compton down-scatterings and thus lost a significant or dominant fraction of their initial energy due to electron recoils. The emergent hard X-ray spectrum has thus lost much of the memory about its parent emission processes and as a result is fairly similar to the Comptonized spectra appearing in various astrophysical situations where hard X-rays or gamma-rays propagate through a dense and cold environment, e.g. in supernovae (Grebenev & Sunyaev 1987). In particular, such a spectrum was observed from SN 1987A (Sunyaev et al. 1987).

2.1.1 Adequacy of the adopted atmosphere model

Our using of a plane-parallel model for the Earth’s atmosphere is motivated by the fact that all of typical free paths of particles and photons in the problem under consideration are less than a few ten km and are thus much shorter than

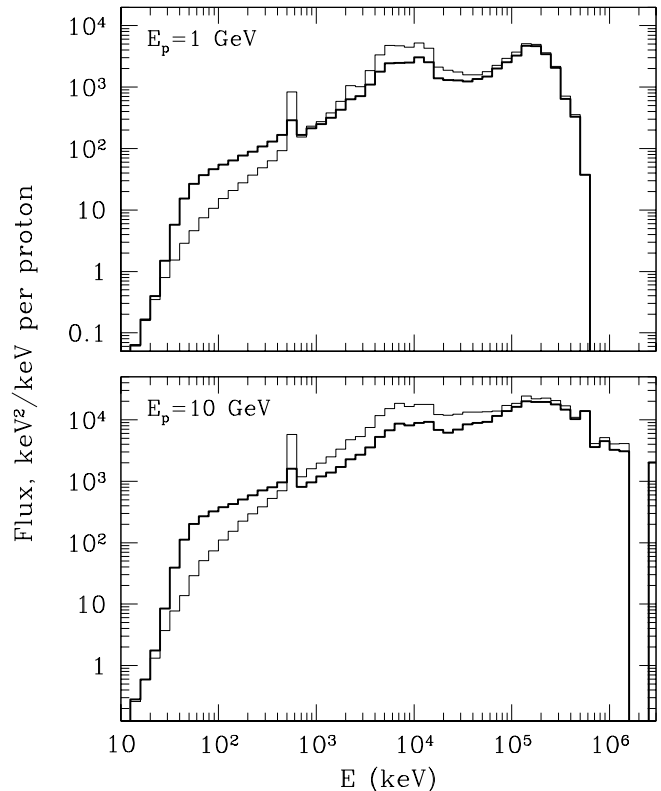


Figure 2. *Top:* Spectral energy distribution (in $E^2 dN_\gamma/dE$ units, thick solid line) of photons emergent from the atmosphere exposed from the top to an isotropic distribution of protons of energy $E_p = 1$ GeV. The thin line shows the spectrum of the initial energies (i.e. before Comptonization) of the escaping photons. *Bottom:* The same but for $E_p = 10$ GeV.

the Earth radius. Nevertheless, to verify the adequacy of the adopted approximation we performed a series of more realistic simulations, in which the Earth’s atmosphere was modeled as a spherical shell with an inner radius of 6400 km and an outer radius of 6496 km. The vertical structure and chemical composition of the atmosphere were adopted exactly the same as in our reference (slab-geometry) model. In Fig. 3 we compare the angular-integrated emergent spectrum produced by 1 GeV protons in the spherical atmosphere with that produced in the plane-parallel one. As expected, there is no significant difference between these two spectra apart from the statistical noise. We found this to be the case also for other incident proton energies. These results confirm that the plane-parallel approximation is appropriate for our study (see also Sect. 2.1.3 below).

We also show in Fig. 3 a simulated spectrum for a plane-parallel atmosphere that has the same sea-level density (1.2 mg cm^{-3}) and scale-height (8 km) as our reference model but is only 48 km (instead of 96 km) high. In this case too there are no significant deviations in the outgoing spectrum relative to the one computed within our standard model. We present this example to demonstrate the very weak sensitivity of the emergent spectrum to changes in the

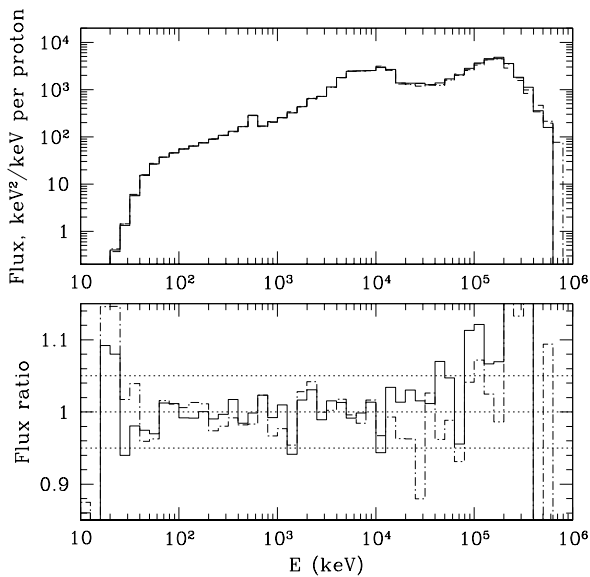


Figure 3. *Top:* Spectral energy distribution (in $E^2 dN_\gamma/dE$ units) of photons emergent from the atmosphere exposed from the top to an isotropic distribution of protons of energy $E_p = 1$ GeV for different models of the atmosphere: a slab geometry with a total height of 96 km (the reference model) – the dashed line, a spherical shell geometry with an inner radius of 6400 km and the same vertical structure as the reference model – the dashed line, and a slab geometry with a total height of 48 km and the same vertical structure as the lower half of the reference model – the dash-dotted line. *Bottom:* The ratio of the spectra obtained for the spherical and 48-km slab models to that obtained for the reference model – the solid and dash-dotted line, respectively.

setup of the atmosphere other than its chemical composition, which was mentioned at the beginning of Sect. 2.

In addition, Fig. 3 provides a sense of the statistical uncertainties pertaining to our simulations, which, as we have already mentioned, are at the level of a few per cent over the 25 keV–10 MeV energy range.

2.1.2 Fitting formulae for the emergent hard X-ray spectrum

On performing many simulations, we proved (see Fig. 4) that the emergent spectrum between 25 and 300 keV is barely sensitive to the energy of the parent cosmic proton in the range of interest to us, namely from ~ 400 MeV to ~ 250 GeV (see Sect. 3). The outgoing photon spectrum over 25–300 keV can be well approximated by the following fitting formula:

$$\frac{dN_\gamma}{dE} = \frac{C}{(E/44 \text{ keV})^{-5} + (E/44 \text{ keV})^{1.4}} \text{ keV}^{-1}, \quad (1)$$

where the coefficient C depends on the primary particle energy as is discussed below.

The photon spectrum (Fig. 4) peaks at ~ 50 –60 keV. At energies below 40 keV the spectrum exhibits a rapid decline

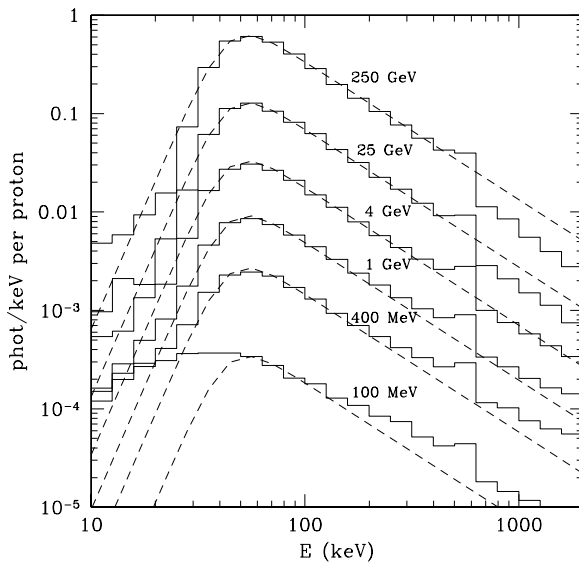


Figure 4. Emergent spectra (solid lines, note the different units compared to the previous figures) in the X-ray to soft gamma-ray range for different energies of incoming cosmic protons (labels next to the curves). The dashed lines show the analytic approximation for the 25–300 keV range given by equation (1). This approximation breaks down at $E_p \lesssim 400$ MeV.

($\propto E^5$) due to Compton down-scatterings. Above ~ 300 –400 keV, where the escaping photons have experienced at most few Compton scatterings, the spectrum (including the strength of the 511 keV line) starts to exhibit a noticeable dependence on the incident proton energy. This is also the case for photons with energies less than ~ 25 keV, most of which were born via bremsstrahlung in the skin of the atmosphere with surface density \sim several g cm^{-2} and whose spectrum retains signatures of the energy distribution of the parent secondary electrons. We note that at these low energies the emergent X-ray flux is very weak due to photoabsorption.

We next address the amplitude of the resulting photon spectra. In Fig. 5 the coefficient C appearing in equation (1) is shown as a function of the incident proton energy E_p . The results of simulations in the range 400 MeV–250 GeV are well described by the following expression:

$$C_p(E_p) = \frac{0.0166}{(E_p/0.6 \text{ GeV})^{-1.8} + (E_p/0.6 \text{ GeV})^{-0.7}}, \quad (2)$$

which allows one to calculate the emergent intensity for a given incident spectrum of cosmic protons, as we do in §3 below.

2.1.3 Angular dependence of emergent radiation

We proceed to compare spectra emergent at different zenith angles. We found (see Fig. 6) that the spectral shape between 25 and 300 keV remains stable and as given by equation (1), while the flux (Fig. 7) approximately obeys the law

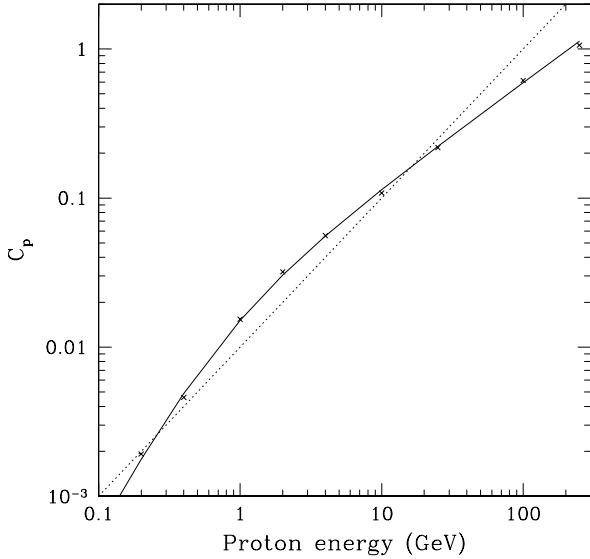


Figure 5. Normalization of the emergent 25–300 keV spectrum, equation (1), as a function of proton energy E_p . Shown are values derived from simulations (points) and the fitting curve (solid) given by equation (2). An arbitrarily scaled linear dependence is shown for comparison (dotted).

$$dF \propto \mu(1 + \mu)d\mu. \quad (3)$$

This means that the outgoing hard X-ray radiation exhibits some central brightening as compared to the classical Lambert case, $dF \propto \mu d\mu$, corresponding to black-body radiation. The angular distribution of the atmospheric hard X-ray emission is also different from the law of darkening pertaining to the other classical case of a semi-infinite scattering atmosphere with radiation coming from deep interiors: $dF \propto \mu(1 + 2\mu)d\mu$ (Chandrasekhar 1960; Sobolev 1963). The resulting distribution actually resembles that of the Comptonized radiation escaping from a purely scattering disk with optical thickness $\tau_T \sim$ a few (Titarchuk & Sunyaev 1985). This reflects the fact that although cosmic rays generate radiation over several hundred g cm^{-2} deep into the atmosphere, only radiation produced in the top few ten g cm^{-2} of air can efficiently survive multiple Compton downscatterings (as well as photoabsorption) and escape into space in the form of hard X-rays.

On the contrary, the emergent gamma-rays (with energies $\gtrsim 1\text{--}2$ MeV) exhibit some limb brightening (enhanced flux at small μ 's and reduced flux at large μ 's), see the bottom panel of Fig. 7), which can be attributed to the fact that escaping gamma quanta have experienced at most a few Compton scatterings.

In Fig. 7 we also compare the result obtained using our standard atmosphere model with one computed using the spherical setup of the atmosphere, described in Sect. 2.1.1. Similarly to the angular-integrated spectrum, there are no significant differences between the two derived angular dependences of the emergent flux. Specifically, the difference

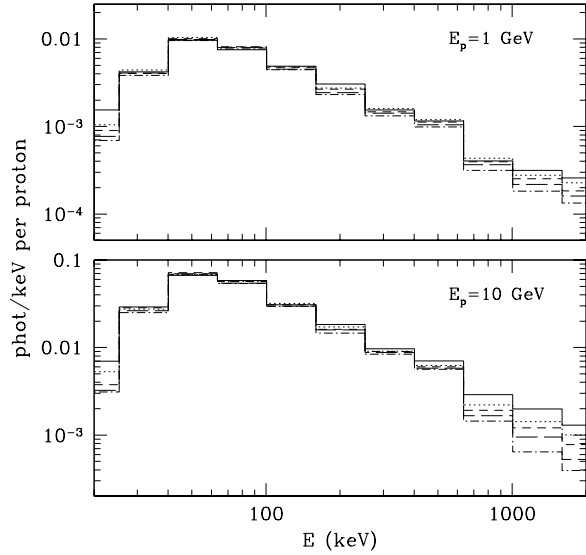


Figure 6. *Top:* Spectra for $E_p = 1$ GeV, emergent at different zenith angles ($\mu = \cos \theta$): $\mu = 0\text{--}0.2$ (solid), $0.2\text{--}0.4$ (dotted), $0.4\text{--}0.6$ (short-dashed), $0.6\text{--}0.8$ (long-dashed) and $0.8\text{--}1.0$ (dash-dotted). The spectra were divided by $\mu(1 + \mu)$. *Bottom:* The same but for $E_p = 10$ GeV.

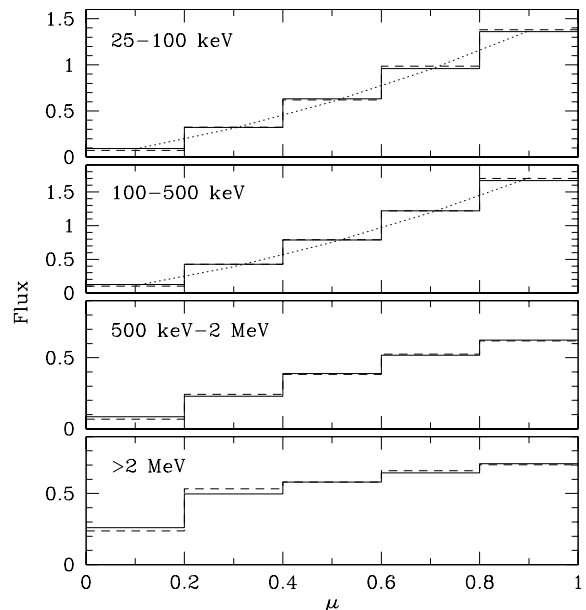


Figure 7. Emergent flux for $E_p = 10$ GeV as a function of the zenith angle ($\mu = \cos \theta$) in different photon energy ranges: 25–100 keV, 100–500 keV, 500 keV–2 MeV and above 2 MeV. The solid and dashed lines show the results obtained using the plane-parallel and spherical atmosphere models. In the upper two panels also a well-matching $\sim \mu(1 + \mu)$ dependence is shown (dotted).

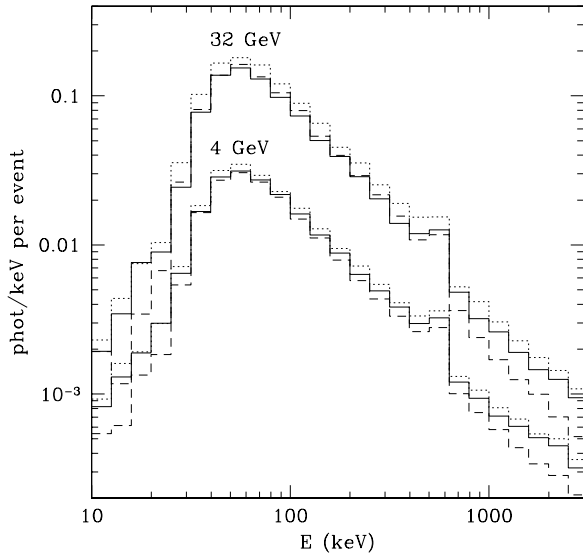


Figure 8. Emergent spectra in the X-ray to soft gamma-ray range generated by α -particles of energy $E_\alpha = 4$ and 32 GeV (solid lines) compared to the spectra generated by protons of energy $E_p = E_\alpha$ (dashed lines) and by four protons each of energy $E_p = E_\alpha/4$ (dotted lines).

between the two approximations is less than 3% of the average flux, $\langle dF/d\mu \rangle$, in each bin including the $0 < \mu < 0.2$ one (corresponding to zenith angles between 78.5° and 90°). We do expect though the plane-parallel approximation to eventually break down at grazing angles approaching 90° . However, at these angles only a tiny fraction of the total flux from the Earth is emitted (for example the fraction of the total flux emitted at $\mu < 0.2$ is $\sim 3\%$), which implies that our plane-parallel model should be applicable to virtually any space-born experiment.

2.2 Alpha particles

A major component of Galactic cosmic rays is He nuclei. *GEANT4* permits to handle inelastic scatterings of α -particles up to $E_\alpha \sim 40$ GeV. We therefore ran a number of simulations of bombardment of the atmosphere by monoenergetic α -particles and found (see Fig. 8) that the resulting hard X-ray spectra are nearly identical to those induced by protons of the same energy as the α -particles ($E_p = E_\alpha$). If the spectrum generated by an α -particle of energy E_α is instead compared with that generated by four protons each of energy $E_p = E_\alpha/4$ (a possibility suggested by the simplest superposition theory), then the match becomes somewhat worse. We can therefore extend the use of equation (2), originally derived for protons, to α -particles, in which case one should simply substitute E_α for E_p in the formula.

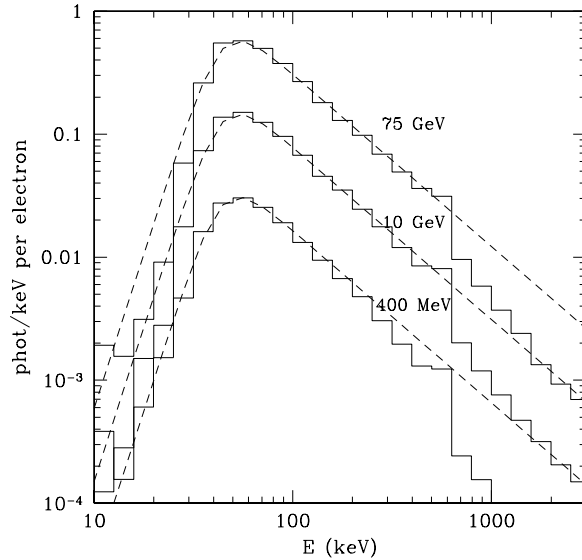


Figure 9. Emergent spectra (solid lines) in the X-ray to soft gamma-ray range generated by cosmic electrons of different energies. The dashed lines show the analytic approximation in the 25–300 keV range given by equation (1).

2.3 Cosmic electrons and positrons

A significant fraction of Galactic cosmic rays consists of electrons (with a small fraction of positrons). We therefore also performed simulations for monoenergetic electrons. The resulting hard X-ray spectra are not significantly different from the case of protons and in the energy band 25–300 keV equation (1) remains a good approximation of the spectra (Fig. 9). We also tested positrons and, as expected, obtained nearly identical results.

In Fig. 10 the spectral normalization C_e – to be substituted for C in equation (1) – is shown as a function of the electron energy E_e . This dependence can be approximated as

$$C_e(E_e) = 0.072 \left(\frac{E_e}{\text{GeV}} \right)^{0.4} \left[1 + 0.07 \left(\frac{E_e}{\text{GeV}} \right)^{0.69} \right]. \quad (4)$$

Similarly to the case of protons, in §3 below we integrate equation (4) over the energy spectrum of cosmic electrons bombarding the Earth.

2.4 Re-entrant albedo particles

So far we have implicitly assumed that only energetic particles coming from space can induce X-ray and gamma-ray emission in the atmosphere. However, already early studies (e.g. Puskin 1970) indicated that additional radiation should be generated by re-entrant albedo particles, i.e. secondary electrons and positrons that were born in air showers, escaped from the atmosphere but were then deflected back into it by the geomagnetic field. Although an accurate evaluation of this effect would require more detailed sim-

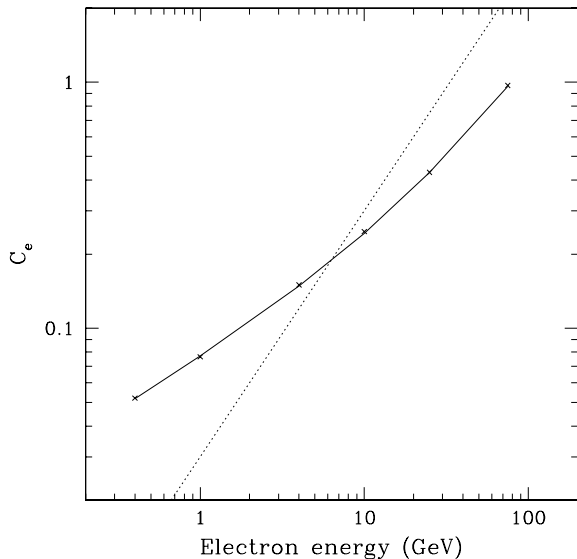


Figure 10. Normalization of the emergent 25–300 keV spectrum, equation (1), as a function of electron energy E_e . Shown are values derived from simulations (points) and the fitting curve (solid) given by equation (4). An arbitrarily scaled linear dependence is shown for comparison (dotted).

ulations involving magnetic fields, it is possible to make a first-order estimate. For this purpose, we used the recorded spectra of secondary electrons and positrons induced by cosmic protons and emergent from the atmosphere (Fig. 1) as new input spectra for bombarding the atmosphere. This is a reasonable procedure since the low magnetic rigidities (momenta per charge) of most of these particles (< 1 GV) do not allow them to escape into interplanetary space.

In Fig. 11 we show the emergent photon spectra generated by re-entrant particles in comparison with the previously computed spectrum formed during the primary proton-induced cascade. It can be seen that the spectral shape of the secondary components produced by re-entrant electrons and positrons in the 25–300 keV range is not significantly different from that of the primary spectrum and that re-entrant particles contribute together $\sim 8\%$ to the hard X-ray flux. Moreover, we verified that this amount depends very little on the primary proton energy. We take this minor additional component into account when making our final predictions in §3.

We also explored the contribution of re-entrant albedo particles generated by primary cosmic electrons. The corresponding additional hard X-ray flux proves to be less than 1% of the flux generated by the primary electrons, i.e. $\lesssim 10^{-3}$ of the flux due to cosmic protons, and thus can be neglected.

3 PREDICTIONS FOR OBSERVATIONS

In the preceding section we demonstrated that cosmic particles of different types and energies generate in the Earth's

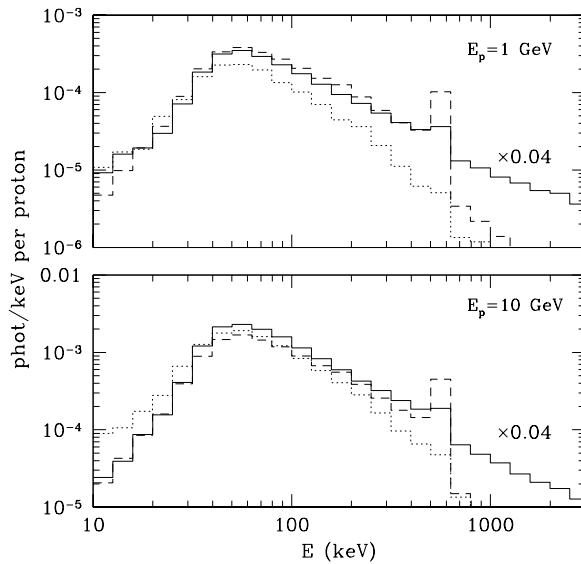


Figure 11. *Top:* Emergent spectra produced by the re-entrant albedo electrons (dotted) and positrons (dashed) generated by protons of energy $E_p = 1$ GeV. The spectrum produced during the primary cascade, multiplied by 0.04, is shown for comparison (solid line). *Bottom:* The same but for $E_p = 10$ GeV.

atmosphere hard X-ray radiation with a nearly universal spectrum, which can be approximately described by equation (1). We also determined the dependence of the emergent flux on the primary particle energy. On the other hand, the spectrum and chemical composition of Galactic cosmic rays impinging on the Earth³ are known to a good accuracy, in particular thanks to the many experiments of the past decade. The spectrum is stable at high energies (above ~ 10 GeV per nucleon) but varies significantly at lower energies over the 11-year solar cycle due to modulation by the interplanetary magnetic field and solar wind, as well as with position on the Earth due to a rigidity cutoff imposed by the terrestrial magnetosphere. Since these effects are fairly well understood, we can combine the available information about the cosmic-ray spectrum with the results of our simulations for monoenergetic particles (§2) to make predictions for observations of the Earth's hard X-ray radiation by satellite-born instruments.

3.1 Integrating over the cosmic-ray spectrum

To describe the spectrum of cosmic protons as well as its dependence on the solar modulation potential ϕ ($Ze\phi$ corresponds to the average energy loss of cosmic rays inside the heliosphere, where Z is the charge number of a particle and e is the electron charge), we use the approximation provided

³ Note that after solar flares the Earth is bombarded by additional cosmic rays with variable spectrum. This transient component is not considered here.

by Usoskin et al. (2005), which is based on a summary of recent measurements. Specifically, we adopt for the differential spectrum of protons at 1 AU

$$J_p(E, \Phi) = \frac{1.9[(E + \Phi)(E + \Phi + 1.876)]^{-1.39}}{1 + 0.4866[(E + \Phi)(E + \Phi + 1.876)]^{-1.255}} \times \frac{E(E + 1.876)}{(E + \Phi)(E + \Phi + 1.876)} \text{ particles (s cm}^2 \text{ sr GeV/nucleon)}^{-1}, \quad (5)$$

where E (GeV) is the kinetic energy per nucleon and Φ (GeV) = $(Ze/A)\phi$ (here A is the atomic mass), so that for protons $E = E_p$ and $\Phi = e\phi$. We refer the reader to the above-mentioned paper (see also e.g. Gaisser et al. 2001) for references to the original data from the experiments AMS, BESS, CAPRICE, IMAX, MASS, etc, most of which agree with each other within $\sim 10\%$ at energies below ~ 200 GeV.

The Galactic cosmic-ray spectrum is additionally modified by the geomagnetic field. To a first approximation, adopted below, this modulation can be represented by a sharp cutoff below a certain value R_{cut} (GV) of the magnetic rigidity of a charged particle, whose dependence on the geomagnetic coordinates is well-known. In §3.3 below we estimate the systematic error associated with this approximation.

Proceeding with our analysis, we integrated the approximation for C_p given by equation (2) over the spectrum of cosmic protons given by equation (5) for specified values of the solar modulation potential ϕ and geomagnetic cutoff rigidity R_{cut} . The integration was done up to $E_p = 1000$ GeV, protons with energies higher than 250 GeV contributing $\sim 3\%$ to the emergent radiation flux for the highest expected values of $R_{\text{cut}} \sim 15$ GV and less for lower cutoff values.

In Fig. 12 we show the predicted hard X-ray flux induced by cosmic protons as a function of R_{cut} for two values of ϕ : 0.5 and 1.5 GV, which are typical for solar minima and maxima, respectively (when the suppression of the low energy cosmic-ray flux is weakest and strongest, respectively). One can see that the emergent hard X-ray flux is almost independent of R_{cut} when $R_{\text{cut}} \lesssim 1$ GV, as could be expected since the flux of incident protons with rigidities below ~ 1 GV is strongly suppressed by solar modulation. As follows from Fig. 12, the emergent hard X-ray flux is expected to increase by a factor of ~ 2 during solar minima compared to solar maxima in regions with low geomagnetic cutoff rigidity, i.e. near the magnetic poles of the Earth. The solar-cycle variations become progressively smaller with increasing cutoff rigidity and reduce to $\sim 10\%$ near the geomagnetic equator, where $R_{\text{cut}} \sim 15$ GV.

We next performed a similar calculation for α -particles. In this case the Galactic spectrum is very similar to that of protons, while He composes $\sim 5\%$ (in particle number) of cosmic rays. The solar-modulated spectrum of α -particles can thus be well approximated by equation (5) multiplied by 0.05 (Usoskin et al. 2005). Note that since for a given particle energy the rigidity of α -particles is a factor of ~ 2 smaller than that of protons, the effects of the solar and geomagnetic modulation are accordingly modified. The results of §2 indicate that the radiation flux produced by an α -particle of given energy is nearly equal to that induced by a proton of the same energy (at least at energies below 40 GeV).

This makes the corresponding calculation straightforward. In Fig. 12 we show as a function of R_{cut} (geomagnetic cutoff rigidity for a proton) the predicted hard X-ray surface brightness of the Earth's atmosphere due to bombardment by α -particles during solar minimum and maximum. The hard X-ray flux induced by α -particles proves to be $\sim 22\%$ and $\sim 28\%$ at $R_{\text{cut}} \lesssim 1$ GV and $R_{\text{cut}} \gg 1$ GV, respectively, of that due to protons.

We can estimate in the same manner the contribution of heavier cosmic particles. To this end we assume that atoms of the groups CNO, Ne-S and Fe have the same Galactic spectra as α -particles and protons, while their differential fluxes (per GeV/nucleon) are 6.8%, 2.6% and 0.54% of that of α -particles (e.g. Fiorentini et al. 2001). Since for these groups of atoms the relation $Z = A/2$ approximately holds, the helio- and geomagnetic effects for them are similar to the case of He. Assuming that, similarly to the case of He, the hard X-ray flux induced by a heavy particle is the same as that produced by a proton of equal energy, the hard X-ray surface brightness of the Earth's atmosphere due to bombardment by heavy cosmic particles can be readily estimated (Fig. 12).

We can next estimate the hard X-ray surface brightness of the atmosphere due to bombardment by cosmic electrons and positrons. In this case we should use equation (4) instead of equation (2). Also the magnetic rigidity effects are somewhat different from the case of protons and nuclei because the rest energy of electrons and positrons is negligible. Adopting for the solar-modulated spectrum of cosmic electrons (Webber et al. 1983)

$$J_e(E_e, \phi) = 0.07(E_e + e\phi)^{-3.3} \left(\frac{E_e}{E_e + e\phi} \right)^2 \text{ (s cm}^2 \text{ sr GeV)}^{-1}, \quad (6)$$

we obtain the dependence of the emergent hard X-ray flux on R_{cut} shown in Fig. 12.

Finally, the contribution of re-entrant albedo electrons and positrons can be roughly estimated by multiplying the hard X-ray flux due to cosmic protons and nuclei by 0.08 (see §2.4), since albedo particles are expected to re-enter the atmosphere in the opposite geomagnetic hemisphere in regions with similar geomagnetic cutoff rigidity to their escape positions. This emission component as well as the total atmospheric signal are shown as functions of R_{cut} in Fig. 12.

3.2 Approximate formula for the hard X-ray surface brightness of the Earth's atmosphere

We found that over the region of practical interest: $0.3 < \phi(\text{GV}) < 2$ and $R_{\text{cut}}(\text{GV}) \lesssim 50$ – the dependence of the atmosphere's hard X-ray surface brightness on the solar modulation potential ϕ , geomagnetic cutoff rigidity R_{cut} and zenith angle θ ($\mu = \cos\theta$) can be well described by the following formula:

$$C = \frac{3\mu(1 + \mu)}{5\pi} \frac{1.47 \times 0.0178 [(\phi/2.8)^{0.4} + (\phi/2.8)^{1.5}]^{-1}}{\{1 + [R_{\text{cut}}/(1.3\phi^{0.25}(1 + 2.5\phi^{0.4}))]^2\}^{0.5}} \text{ (s cm}^2 \text{ sr)}^{-1}. \quad (7)$$

To calculate the emergent hard X-ray spectrum (from 1 cm^2 of the Earth's atmosphere into a unit solid angle) for given

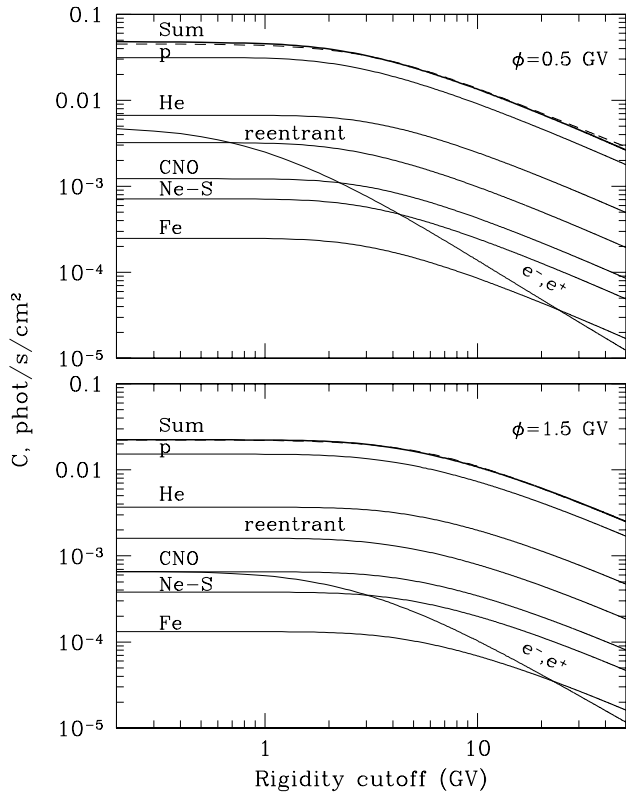


Figure 12. *Top:* Predicted hard X-ray surface brightness (integrated over all zenith angles) of the Earth's atmosphere during solar minimum ($\phi = 500$ MV) as a function of the geomagnetic cutoff rigidity (for a proton) R_{cut} . The thick solid line shows the expected total signal – coefficient C in the spectral approximation given by equation (1), which consists of several components (thin solid lines): due to protons, α -particles, CNO nuclei, Ne-S nuclei, Fe nuclei, cosmic electrons and positrons, and re-entrant electrons and positrons. The cumulative flux is well fit by equation (7) – the dashed line nearly coincident with the thick solid line. *Bottom:* The same but for solar maximum ($\phi = 1.5$ GV).

values of ϕ , R_{cut} and μ , one just needs to substitute the amplitude C given by equation (7) into equation (1).

We first derived the above dependence for protons only and then proved that the combined contribution of the other cosmic-ray constituents, despite their somewhat different dependences on R_{cut} (see Fig. 12), can be well represented by the additional factor 1.47 appearing in equation (7). This factor also takes into account the estimated $\sim 8\%$ contribution of re-entrant albedo particles.

To verify our prediction for the atmospheric hard X-ray spectrum given by equations (1) and (7), we performed a series of simulations where the atmosphere was bombarded by the cosmic proton spectrum expected for specified (ϕ , R_{cut}) values according to equation (5). In Fig. 13 we present two extreme examples of the resulting emission spectra – one corresponding to observing a geomagnetic pole during solar minimum and the other to observing the geomagnetic equator during solar maximum, in both cases on integrat-

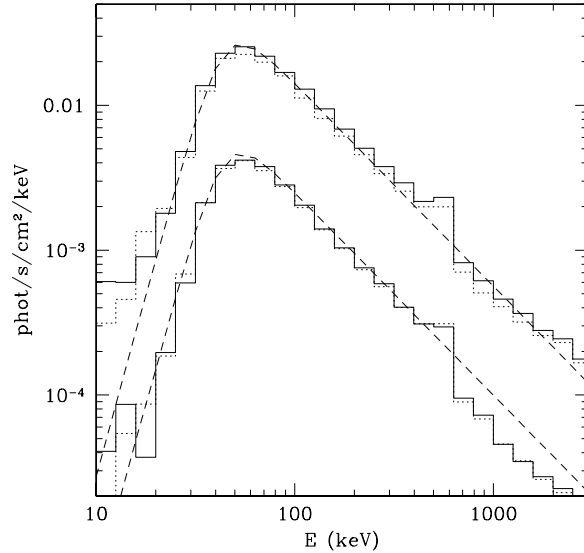


Figure 13. Simulated spectra (solid lines) of Earth atmospheric emission induced by cosmic protons for $\phi = 0.5$ GV, $R_{\text{cut}} = 0.5$ GV and $\phi = 1.5$ GV, $R_{\text{cut}} = 15$ GV (upper and lower curves, respectively). The dashed lines show the corresponding predictions for the 25–300 keV energy range based on equations (1) and (7) (integrated over all zenith angles). The dotted lines are simulations based on the incident direction-dependent cutoff rigidity approach in the dipole approximation for the geomagnetic field ($R_{\text{cut}} = 0.5$ GV and $R_{\text{cut}} = 15$ GV approximately correspond to $\lambda_m = 64.6^\circ$ and 0° , respectively). All the simulated spectra were multiplied by 1.47 to account for the non-proton cosmic rays and re-entrant albedo particles.

ing the outgoing radiation over all zenith angles. It can be seen that the computed spectra are in very good agreement with our analytic prediction in the 25–300 keV energy range. This confirms the self-consistency of our treatment and the stated few per cent statistical accuracy of our simulations.

3.3 Effect of the cutoff rigidity's zenith angle dependence

In the preceding discussion we assumed that at a given position on the Earth the geomagnetic cutoff rigidity is the same for all directions of incidence. In reality, the effects of the geomagnetic field can be better represented by a cutoff rigidity that also depends on the zenith (θ) and azimuthal (ξ) angles. If the geomagnetic field is approximated by a dipole, then the cutoff rigidity is given by Stormer's formula (see e.g. Lipari et al. 1998):

$$R_{\text{cut}} = \frac{M_{\oplus}}{2r^2} \frac{\cos^4 \lambda_m}{[1 + (1 + \cos^3 \lambda_m \sin \theta \sin \xi)^{1/2}]^2}, \quad (8)$$

where $M_{\oplus} \approx 8.1 \times 10^{25}$ G cm³ is the magnetic dipole moment, r is the distance from the dipole center and λ_m is the magnetic latitude. In the atmosphere, i.e. near the Earth surface ($r \approx r_{\oplus}$), $M_{\oplus}/(2r^2) \approx 59.4$ GV, so at the geomag-

netic equator ($\lambda_m = 0$) R_{cut} takes values between 10.2 and 59.4 GV, the vertical ($\theta = 0$) cutoff being 14.9 GV; at the poles $R_{\text{cut}} = 0$ for all directions.

We ran a series of simulations where for given values of the solar modulation potential ϕ and geomagnetic latitude λ_m the incident cosmic-proton spectra were dependent on the zenith and azimuthal angles, namely they were cut off at R_{cut} according to equation (8). We then compared the produced spectra of atmospheric hard X-ray emission with those simulated assuming that regardless of the incident direction the proton spectrum is truncated at the vertical cutoff value: $R_{\text{cut}}(\lambda_m, \theta, \phi) = R_{\text{cut}}(\lambda_m, \theta = 0)$. Both kinds of spectra turned out to be mutually consistent within a few per cent (see Fig. 13), even at the geomagnetic equator. We note however that Stormer's formula generally underestimates the cutoffs because it allows penetration of charged particles with trajectories that would have intersected the surface of the Earth (Smart & Shea 2004). The emergent radiation flux may thus be smaller than predicted here by a few per cent. More accurate simulations should be based on a particle backtracking approach and use more realistic models of the geomagnetic field.

3.4 Observations of the Earth from space by a wide-field instrument

Equation (7) allows one to predict the hard X-ray surface brightness of the atmosphere or its part when observed from a spacecraft, provided that its orbit is higher than ~ 50 –100 km. As a practical example, we may use this formula to predict the hard X-ray flux that would be measured by a satellite-born instrument whose field of view covers the entire terrestrial disk, which was the case in the recent INTEGRAL observations. In the dipole approximation for the Earth's magnetosphere, the spectral coefficient C in equation (1) can be calculated as a function of the spacecraft geomagnetic latitude λ_m and altitude D (Fig. 14). One can see that in the case of a low orbit ($D = 400$ km in our example), during solar minimum the flux detected during the passage of one of the magnetic poles (λ_m) will be ~ 5 times higher than that measured during the passage of the equator. In the case of intermediate and high orbits (20,000 and 200,000 km in our examples) the relative amplitude of variations is expected to be ~ 2 .

We point out that since the geomagnetic field is not exactly dipolar, in analyzing the data from a real experiment one should integrate equation (7) over the geomagnetic rigid-body map corresponding to a given observation.

4 HARD X-RAY RADIATION FROM THE MOON AND PLANETS

Obviously, the same mechanism of hard X-ray production should work in the crust of the Moon, so it is interesting to consider this case as well. Since the Moon has a negligible magnetic field, in its case both the incident cosmic-ray flux and the emergent hard X-ray flux are expected to depend on the solar cycle phase only.

We performed simulations assuming that the Moon's crust has a density of 3 g cm^{-3} and consists of O, Si, Al, Fe, Ca, Mg, and Ti with mass fractions of 43, 21, 10, 10, 9, 5 and

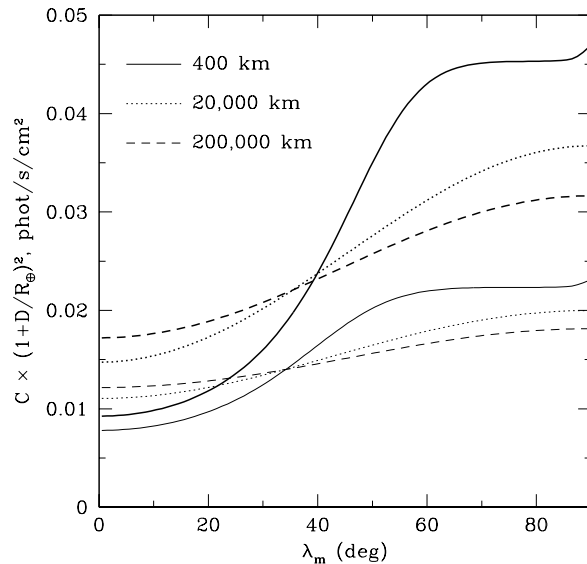


Figure 14. Hard X-ray spectral flux – coefficient C in equation (1) – that would be detected from the whole Earth by a wide-field instrument in different circular orbits (see notation on the figure), as a function of the spacecraft geomagnetic latitude. The thick and thin lines correspond to observations during solar minimum ($\phi = 0.5$ GV) and solar maximum ($\phi = 1.5$ GV), respectively. Note that the dependencies were rescaled as indicated along the vertical axis.

2%, respectively. It turns out (see Fig. 15) that the spectrum emitted above ~ 100 keV is similar to that produced in the Earth's atmosphere and only the cutoff below 100 keV is stronger due to photoabsorption on heavy atoms. The Moon's spectral surface brightness can be approximated in the energy range 40–300 keV as follows:

$$\frac{dN_\gamma}{dE} = \frac{3\mu(1+\mu)}{5\pi} \times 0.013 \left[\left(\frac{\phi}{2.8} \right)^{0.4} + \left(\frac{\phi}{2.8} \right)^{1.5} \right]^{-1} \left[\left(\frac{E}{88 \text{ keV}} \right)^{-4.5} + \left(\frac{E}{88 \text{ keV}} \right)^{1.2} \right]^{-1} (\text{s cm}^2 \text{ sr keV})^{-1}. \quad (9)$$

In writing down this formula we assumed, by analogy with the Earth's atmosphere, that the total radiation flux produced in the Moon's crust is that due to primary cosmic protons times 1.4. Note that the corresponding factor for the Earth's atmosphere (1.47) included the small contribution of re-entrant albedo particles.

Similar results are expected also for Mars and Mercury, since the chemical composition of their solid crusts is similar to that of the Moon and they too have thin gaseous atmospheres and weak magnetospheres. Also the effects of interplanetary magnetic fields on the flux of cosmic rays are not expected to be significantly different in the orbits of Earth, Mars and Mercury.

Interestingly, the Moon should appear as a fairly bright hard X-ray source when observed from a satellite orbiting

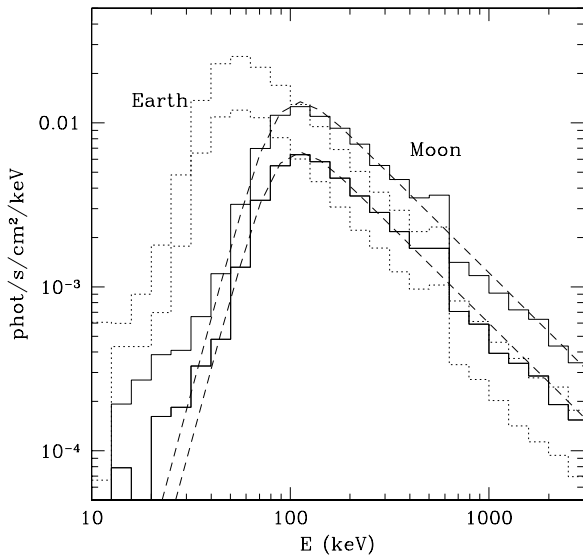


Figure 15. Expected spectra of cosmic ray-induced emission from the Moon’s crust (integrated over all zenith angles) during solar minimum ($\phi = 0.5$ GV) and maximum ($\phi = 1.5$ GV) – upper and lower histogram, respectively. The dashed lines show the approximation in the 25–300 keV energy range given by equation (9). For comparison shown are the corresponding spectra emitted near the magnetic poles of the Earth ($R_{\text{cut}} = 0$).

the Earth. Indeed, on integrating equation (9) over the Moon disk one finds that a detector located at distance D from the Moon will measure a spectral flux

$$F_{\text{Moon}}(D) = (4 \div 8) \times 10^{-7} \left(\frac{3 \times 10^5 \text{ km}}{D} \right)^2 \times \left[\left(\frac{E}{88 \text{ keV}} \right)^{-4.5} + \left(\frac{E}{88 \text{ keV}} \right)^{1.2} \right]^{-1} \frac{\text{photon}}{\text{s cm}^2 \text{ keV}}, \quad (10)$$

where the lower and upper values correspond to observations during solar maximum and minimum, respectively. Therefore, a flux of ~ 1 mCrab is expected at 100–200 keV.

One can expect hard X-ray production by cosmic rays to be much less efficient on giant planets such as Jupiter and Saturn, since their typical cutoff rigidities (roughly proportional to the product of the magnetic field strength on the surface of the planet and its radius) are much higher than in the terrestrial case. Similarly, the spectrum of Galactic cosmic rays impinging on the Sun is truncated at TeV energies (Seckel et al. 1991), and this strongly suppresses the generation of hard X-rays and gamma-rays in the solar atmosphere.

5 DISCUSSION AND CONCLUSIONS

We have revisited the problem of the X-ray and gamma-ray emissivity of the Earth’s atmosphere taking advantage of the

recent high-quality measurements of the Galactic cosmic-ray spectra and the availability of efficient Monte Carlo codes incorporating state-of-the-art descriptions of hadronic physics and electromagnetic cascades. We found that emission generated in the energy band 25–300 keV has a practically invariant spectral shape and a flux that is expected to show significant variations both with time (over the solar cycle) and with position on the Earth (due to geomagnetic effects). We provided two simple expressions – equations (1) and (7) – which allow one to predict the spectral intensity of atmospheric hard X-ray emission for a particular observation from a spacecraft. It should be noted that our results are not directly applicable to observations performed from balloons floating at altitudes below ~ 50 km, since then in addition to the upward flux there will also be a significant amount of downward radiation generated in the several overlying g cm^{-2} of air.

The statistical accuracy of our predictions is better than 5%, while the systematic uncertainty is probably dominated by the current uncertainty in our knowledge of the cosmic-ray flux, which is $\sim 10\%$. We can try to assess the overall accuracy of our model through direct comparison with real observations of the Earth from spacecraft. Among the few published measurements of atmospheric emission in the hard X-ray domain are those done in the 1970’s from the satellites Kosmos 461 (Golenetskii et al. 1974) and 1972-076B (Imhof et al. 1976). The spectra obtained in the energy range ~ 50 –1000 keV could be well described by a power law with a photon index ($dN_{\gamma}/dE \propto E^{-\Gamma}$) $\Gamma = 1.55 \pm 0.10$ in the former experiment and $\Gamma \sim 1.31$ –1.47 in the latter. These values are in good agreement with our calculated value of 1.4 for the spectral slope above ~ 50 keV. Furthermore, Golenetskii et al. (1974) (see also Mazets et al. 1975) measured the dependence of the hard X-ray flux on geomagnetic cutoff rigidity over the range $3 < R_{\text{cut}} \text{ (GV)} < 17.5$, and that result too appears to be consistent with our computations.

Recently during a scanning observation of the Earth, the INTEGRAL observatory measured the spectrum of the cosmic X-ray background together with that of atmospheric hard X-ray emission. Our analysis of the data (Churazov et al. 2007) showed that the atmospheric spectrum at energies from ~ 40 to ~ 200 keV is consistent with the prediction of the present study, although the spectral shape was not well constrained by the data. When we adopted the spectral shape given by equation (1), we found the best-fit amplitude of the atmospheric component to lie within 10% of (actually only $\sim 4\%$ higher than) the flux predicted by equation (7) for the relevant value of the solar modulation potential ($\phi = 0.45$ GV) and taking into account the geomagnetic cutoff rigidity map corresponding to the INTEGRAL observations (Churazov et al. 2007).

This good agreement of our model with observations suggests that the Earth could be used as an absolute calibrator of future satellite-born sensitive hard X-ray detectors, complementing the Crab nebula. This possibility as well as the predictive power of our model could be tested soon via new INTEGRAL observations of the Earth performed at a different phase of the solar cycle.

We also demonstrated that under the impact of cosmic rays the solid surfaces of the Moon, Mars and Mercury should be about as bright in hard X-rays as (in fact somewhat brighter than) the Earth’s atmosphere, making

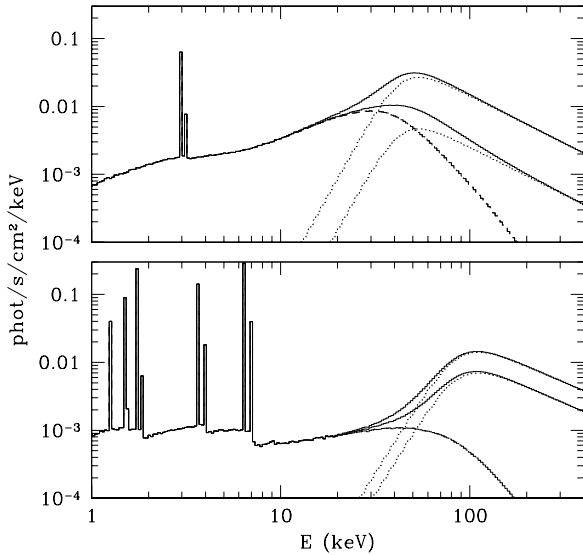


Figure 16. *Top:* Total X-ray spectral surface brightness of the Earth (solid lines) – sum of cosmic ray-induced atmospheric emission (dotted lines) and the reflected CXB radiation (dashed lines). The two sets of curves correspond to observations of a geomagnetic polar region ($R_{\text{cut}} = 0$) during solar minimum ($\phi = 0.5$ GV) and of the geomagnetic equator ($R_{\text{cut}} = 15$ GV) during solar maximum ($\phi = 1.5$ GV). *Bottom:* The same but for the Moon. The two sets of curves correspond to observations performed during solar minimum and solar maximum.

these objects potentially interesting for observations. It is important to keep in mind though that in a real experiment reflected CXB radiation will significantly contribute to the observed signal at energies below ~ 50 keV. Based on the computations of Churazov et al. (2007), we show in Fig. 16 several examples of hard X-ray spectra that could be observed from the Earth and Moon. This figure indicates that the cosmic ray-induced hard X-ray continuum could complement the CXB-induced fluorescent X-ray lines in probing the chemical composition of the crusts of planets and the Moon, i.e. during the Bepi Colombo mission to Mercury⁴.

REFERENCES

Agostinelli S., Allison J., Amako K et al., 2003, Nuclear Instruments and Methods of Physics Research A, 506, 250
 Araújo H.M., Wass P., Shaul D., Rochester G., Summer T.J., 2005, Astroparticle Physics, 22, 451
 Barao F. and AMS-02 Collaboration, 2004, Nuclear Instruments and Methods in Physics Research A 535, 134
 Chandrasekhar S., 1960, Radiative Transfer (Dover, New York)
 Churazov E., Sunyaev R., Revnivtsev M. et al., 2007, A&A, in press; astro-ph/0608250

Churazov, E. Sazonov S., Sunyaev R. et al., 2007, MNRAS, submitted; astro-ph/0608252
 Daniel R.R., Stephens S.A., 1974, Reviews of Geophysics and Space Physics, 12, 233
 Dean A.J., Fan L., Byard K., Goldwurm A., Hall C.J., Harding J.S.J., 1989, A&A, 219, 358
 Fiorentini G., Naumov V., Villante F.L., 2001, Phys. Lett. B, 510, 173
 Gaisser T.K., Honda M., Lipari P., Stanev T., 2001, Proc. 27th Intern. Cosmic Ray Conf., Hamburg, 1643
 Golenetskii S.V., Il'inskii V.N., Mazets E.P., 1974, Cosmic Research, 12, 706
 Graser U., Schönfelder V., 1977, JGR, 82, 1055
 Grebenev S.A., Sunyaev R.A., 1987, Sov. Astron. Lett., 13, 397
 Imhof W.L., Nakano G.H., Reagan J.B., 1976, JGR 81, 2835
 Ling J.C., 1975, JGR, 80, 3241
 Lipari, P., Stanev T., Gaisser T.K., 1998, Physical Review D, 58, 3003
 Mazets E.P., Golenetskii S.V., Il'inskii V.N., Gur'yan Yu. A., Kharitonova, T.V., 1975, Astrophys. & Sp. Sci., 33, 347
 Peterson L.E., Schwarz D.A., Ling J.C., 1973, JGR 78, 7942
 Puskun J.S., 1970, Spec. Rep. 318, Smithsonian Astrophys. Observ., Cambridge, USA
 Ramaty R., Kozlovsky B., Lingenfelter, R.E., 1979, ApJS 40, 487
 Share G.H., Murphy R.J., 2001, JGR, 106, 77
 Shaw S.E., Westmore M.J., Bird A.J., et al., 2003, A&A, 398, 391
 Schönfelder V., Graml F., Penningsfeld F.-P., 1980, ApJ, 240, 350
 Schwartz D.A., Peterson L.E., 1974, ApJ, 190, 297
 Seckel D., Stanev, T., Gaisser T.K., 1991, ApJ, 382, 652
 Smart D.F., Shea M.A., 2004, AdSpR, 36, 2012
 Sobolev V.V., 1963, A Treatise on Radiative Transfer (Van Nostrand, Princeton)
 Sunyaev R., Kaniovsky A., Efremov V., Gilfanov M., Churazov E., Grebenev S. et al., 1987, Nature, 330, 227
 Sunyaev R.A., Titarchuk L.G., 1985, A&A, 143, 374
 Usoskin I.G., Alanko-Huotari K., Kovaltsov G.A., Mursula K., 2005, JGR 110, A12108
 Webber, W.R., 1983, Composition and Origin of Cosmic Rays, ed. M.M. Shapiro (Dordrecht: Reidel)
 Willett J.B., Mahoney W.A., 1992, JGR, 97, 131

⁴ <http://sci.esa.int/home/bepicolombo>